Tenth International Conference on Computational Fluid Dynamics (ICCFD10), Barcelona, Spain, July 9-13, 2018

ICCFD10-2018-0189

Numerical study of combustion stabilization in a Scramjet engine model with cavity flameholder

Fábio H. E. Ribeiro[*,**], Radouan Boukharfane[*], Vincent Robin[*], Arnaud Mura[*]
[*] Pprime Institute UPR 3346 CNRS, ENSMA and University of Poitiers, France
[**] Instituto de Estudos Avançados, São José dos Campos, Brasil
Corresponding author: arnaud.mura@ensma.fr

Abstract: Scramjet engines are high-speed airbreathing propulsion systems that do not require rotating elements to compress the air inlet stream [33]. It is compressed dynamically through a supersonic intake system that is integrated in the forebody, thus leading to the required temperature and pressure levels for combustion to proceed within the combustor length [29]. In such engines, the combustion chamber is crossed by a supersonic flow, which limits the time available to inject fuel, to mix it with oxidizer, to ignite the resulting mixture, and reach complete combustion. Residence times can be increased thanks to cavities, which have the potential to stabilize combustion without excessive total pressure loss and are therefore used as flameholders in supersonic combustors. Flame stabilization mechanism and turbulence-chemistry interactions are studied for a jet in a supersonic crossflow (JISCF) of vitiated air delivering hydrogen upstream of a wall-mounted squared cavity. The corresponding reactive high-speed flow conditions are presently scrutinized on the basis of numerical simulations of a Scramjet model representative of experiments previously conducted at the University of Michigan [22, 24]. The computations are performed with the high-performance computational solver `CREAMS` [18, 19] that has been developed to perform the numerical simulation of compressible reactive multi-component flows on massively-parallel architectures. The solver makes use of high-order precision numerical schemes applied on structured meshes and the combustion chamber geometry is modelled by using a recent immersed boundary method (IBM) algorithm [5]. The present set of computations is conducted within the LES framework and the wall-adapting local eddy (WALE) model is retained as the subgrid-scale viscosity closure. Combustion stabilization is studied for two distinct values of the inlet vitiated airstream temperature. Two stabilization modes are recovered from the numerical simulations: cavity-stabilized regime and jet-wake stabilized regime. Special emphasis is placed on the analysis of the reactive flow topology and structure, as well as combustion regimes, which are analysed on the basis of standard turbulent combustion diagrams.

Keywords: Scramjet, Compressible Flow, High-Speed Flow Combustion, Combustion Stabilization, Large-Eddy Simulation

1 Introduction

Scramjet engine is a very promising propulsion strategy for hypersonic vehicles. One of its main advantages over concurrent technologies is related to the fact that it does not need to carry oxidizer,

which is scooped directly from the atmosphere, thus providing a considerable weight reduction and allowing for higher payloads and specific impulse compared to standard rocket engines [14]. Since it produces no thrust at zero flight speed, such an engine must be ignited after it has been accelerated to its takeover speed thanks to a secondary propulsion system. The issues associated to ignition and propulsion efficiency during this takeover stage are thus important in the Scramjet development but they lie outside the scope of the present study, which is focused on combustion stabilization once significant flight Mach number values are reached.

There are several possible applications of Scramjet engines, including civil high-speed aircrafts, space exploration as reusable stages for access to low Earth orbit, and military hypersonic weapons. Despite many impressive achievements obtained in the field since the early sixties, still today there are no Scramjet engines being used in practical devices: many developments including experimental flights and ground-based testings are currently in progress. In such engines, the combustion chamber is crossed by a supersonic flow, which limits considerably the time available to inject fuel, mix it with the oxidizer, ignite the resulting mixture, and stabilize combustion. Combustion stabilization indeed appears as one of the most challenging issues. One promising solution is the wall-mounted cavity, which has been shown to be quite efficient in stabilizing combustion without excessive total pressure loss [2, 13, 21]. The recirculation zones that develop inside the cavity increase the residence time of intermediate combustion products that can continuously initiate chemical reactions. However, the understanding of the interaction of the fuel jet with the wall-mounted cavity is far from being an easy task and it has motivated a large amount of experimental studies in both reactive and non-reactive conditions. For instance, Ben-Yakar and Hanson [2] investigated hydrogen normal injection in air cross-flow upstream of a cavity simulating in Mach 10 flight conditions. High-speed Schlieren visualization and planar laser-induced fluorescence (OH-PLIF) were used to characterize the compressible flow topology and combustion development. The first OH fluorescence events are found to take place in the recirculation zone upstream of the underexpanded jet and the signal of fluorescence extends further downstream along the outer edge of the jet. Micka and Driscoll [23] studied the combustion characteristics of a dual-mode Scramjet combustor with normal fuel injection upstream of a cavity flame-holder. Depending on the value of the vitiated airstream stagnation temperature, combustion is either anchored at the cavity leading edge and spreads into the main flow at an approximately constant angle (low stagnation temperature levels) or stabilizes a short distance downstream of the hydrogen injection, in its wake, and features a curved leading edge (high stagnation temperature levels). The combustion stabilization is analysed on the basis of premixed flame propagation and the possibility that it flashes forward to a relatively stable location in the hydrogen jet-wake. Sun et al. [30] also analysed combustion in a supersonic combustor with normal hydrogen injection upstream of cavity flame-holders on the basis of experimental investigations using OH-PLIF and numerical simulations performed within an hybrid RANS/LES framework. It is shown that an approximately steady flame may be maintained in the cavity shear layer. Hot combustion products can be transported towards the jet inlet stream through a process of interaction between the counter-rotating vortices issued from the jet and the cavity shear layer.

In the present numerical study, such reactive high-speed flow conditions are scrutinized on the basis of numerical simulations of a Scramjet model representative of experiments previously conducted at the University of Michigan [22, 24]. The purpose is to analyse the reactive flow topology and structure as well as combustion regimes, which are investigated on the basis of standard turbulent combustion diagrams. Combustion stabilization is studied for two distinct values of the inlet vitiated air-stream temperature, which are denoted `RFSC-LST` and `RFSC-HST`, for low- and high-stagnation temperature levels, respectively. The simplified computational geometry consists of a constant section channel, followed by the wall-mounted cavity section, and finally the diverging section. This geometry is handled thanks to the recent IBM algorithm of reference [5]. Two

stabilization modes are recovered from the numerical simulations: cavity stabilization mode for case `RFSC-LST` and jet-wake stabilization mode for case `RFSC-HST`. The manuscript is organised as follows: the LES formalism and numerical methods are presented in the next section. It is followed by a short section §3 where the computational setup is presented and some preliminary verifications reported. The central part of manuscript corresponds to §4, where computational results are analysed in details. Finally, the manuscript ends with a conclusion section, where some perspectives for future works are also presented.

2 Governing equations and numerical methods

2.1 Compressible large-eddy simulation formulation

The closed set of filtered transport equations that has been considered is first presented below. Applying a spatial filter to the set of compressible Navier-Stokes equations requires the introduction of the Favre filter $\widetilde{\phi} = \overline{\rho\phi}/\overline{\rho}$, so as to express non-linear terms into a standard resolved (filtered) part plus a subgrid-scale (SGS) contribution. The set of filtered Navier-Stokes equations are expressed in the following conservative form,

$$\frac{\partial \overline{\rho}}{\partial t} + \frac{\partial \overline{\rho}\widetilde{u}_i}{\partial x_i} = 0 \tag{1}$$

$$\frac{\partial \overline{\rho}\widetilde{u}_j}{\partial t} + \frac{\partial \overline{\rho}\widetilde{u}_i\widetilde{u}_j}{\partial x_i} = -\frac{\partial \overline{p}}{\partial x_j} + \frac{\partial \overline{\tau}_{ij}}{\partial x_i} - \frac{\partial}{\partial x_i}\left(\overline{\rho u_i u_j} - \overline{\rho}\widetilde{u}_i\widetilde{u}_j\right) \tag{2}$$

$$\frac{\partial \overline{\rho}\widetilde{e_t}}{\partial t} + \frac{\partial \overline{\rho}\widetilde{u}_i\widetilde{e_t}}{\partial x_i} = -\frac{\partial \overline{p}\widetilde{u}_i}{\partial x_i} + \frac{\partial \widetilde{u}_i\overline{\tau}_{ij}}{\partial x_j} - \frac{\partial \overline{\mathcal{J}}_i}{\partial x_i} - \frac{\partial}{\partial x_i}\left(\overline{(\rho e_t + p)u_i} - (\overline{\rho}\widetilde{e_t} + \overline{p})\widetilde{u}_i\right) \tag{3}$$

$$\frac{\partial \overline{\rho}\widetilde{Y}_\alpha}{\partial t} + \frac{\partial \overline{\rho}\widetilde{u}_i\widetilde{Y}_\alpha}{\partial x_i} = -\frac{\partial \overline{\rho Y_\alpha V_{\alpha i}}}{\partial x_i} + \overline{\rho}\widetilde{\dot{\omega}}_\alpha - \frac{\partial}{\partial x_i}\left(\overline{\rho Y_\alpha u_i} - \overline{\rho}\widetilde{Y}_\alpha\widetilde{u}_i\right) \tag{4}$$

where t denotes the time, x_j is the Cartesian coordinate in direction j (with $j = 1, \ldots, 3$), u_i is the velocity component in direction i (with $i = 1, \ldots, 3$), ρ is the density, p is the pressure, $e_t = e + u_i u_i/2$ is the total specific energy (obtained as the sum of the internal specific energy, e, and the kinetic energy), and Y_α is the mass fraction of species α (with $\alpha = 1, \ldots, \mathcal{N}_{\text{sp}}$). The integer $\mathcal{N}_{\text{sp}}$ denotes the number of chemical species. The thermodynamic variables are interrelated through the filtered pressure field approximated from $\overline{p} = \overline{\rho}\mathcal{R}\widetilde{T}/\mathcal{W}$, where $\mathcal{R}$ is the gas constant, T denotes the temperature and $\mathcal{W}^{-1} = \sum_{\alpha=1}^{\mathcal{N}_{\text{sp}}} \widetilde{Y}_\alpha/\mathcal{W}_\alpha$ is the molar weight of the multicomponent mixture. In Equation (4), $V_{\alpha i}$ and $\dot{\omega}_\alpha$ denote the αth species diffusion velocity component in direction i and chemical rate, respectively. The filtered stress tensor is evaluated by $\overline{\tau}_{ij} = 2\mu(\widetilde{T})(\widetilde{S}_{ij} - \widetilde{S}_{kk}\delta_{ij}/3)$ with $\widetilde{S}_{ij} = \left(\partial\widetilde{u}_i/\partial x_j + \partial\widetilde{u}_i/\partial x_j\right)/2$ denoting the resolved strain-rate tensor. For the present set of numerical simulations standard modeling assumptions are retained: a mixture-average formulation is retained for the description of the molecular diffusion flux based on a modified version of the Hirschfelder and Curtiss approximation [16]. It is also assumed that both the filtered molecular diffusion flux and the filtered heat flux can be expressed in a way similar to their instantaneous counterparts but applied to filtered quantities. The filtered molecular flux of species α thus writes:

$$\overline{\rho Y_\alpha V_{\alpha i}} \approx \overline{\rho}\widetilde{Y}_\alpha\widetilde{V}_{\alpha i} = -\overline{\rho}\widetilde{D}_\alpha^m \frac{\mathcal{W}_\alpha}{\widetilde{\mathcal{W}}}\frac{\partial \widetilde{X}_\alpha}{\partial x_i} + \overline{\rho}\widetilde{Y}_\alpha\widetilde{V}_i^c \tag{5}$$

where $\widetilde{D}_{\alpha}^{m}$ is the matrix of resolved flux diffusion coefficients of the species α into the mixture. It is worth noting that the last term of Equation (5) is a corrective term that ensures the total mass conservation. At each time step, each correction velocity component $\widetilde{V}_i^c = \sum_{\beta=1}^{\mathcal{N}_{\text{sp}}} \widetilde{D}_{\beta}^{m}(\mathcal{W}_\beta/\widetilde{\mathcal{W}})\partial\widetilde{X}_\beta/\partial x_i$ is evaluated and added to the velocity component $\widetilde{u}_i$ so as to enforce the compatibility between the discrete forms of species mass fractions and total mass conservation equations. In the previous expressions, X_β denotes the molar fraction of the β^{th} species. The i-components of the filtered molecular heat flux is approximated using the same assumption:

$$\overline{\mathcal{J}}_i = -\lambda(\widetilde{T})\frac{\partial\widetilde{T}}{\partial x_i} + \sum_{\alpha=1}^{\mathcal{N}_{\text{sp}}} \overline{\rho}\widetilde{Y}_\alpha\widetilde{V}_{\alpha i}\widetilde{h}_\alpha \tag{6}$$

where λ is the thermal conductivity of the multicomponent mixture as evaluated from the filtered composition and temperature. The subgrid-scale (SGS) stress tensor $T_{ij} = \overline{\rho u_i u_j} - \overline{\rho}\widetilde{u}_i\widetilde{u}_j$ is modeled within the Boussinesq's framework. The deviatoric part of the subgrid stress tensor is thus evaluated from $T_{ij} - T_{kk}\delta_{ij}/3 = -2\mu_{\text{SGS}}(\widetilde{S}_{ij} - \widetilde{S}_{kk}\delta_{ij}/3)$ where $\mu_{\text{SGS}} = \overline{\rho}\nu_{\text{SGS}}$ is the SGS eddy viscosity and T_{kk} denotes the isotropic contribution. The closure of the SGS mass flux relies on a standard turbulent diffusivity assumption, which is expressed in the following general form:

$$T_{\varphi,i} = \overline{\rho\varphi u_i} - \overline{\rho}\widetilde{\varphi}\widetilde{u}_i = \overline{\rho}\left(\widetilde{\varphi u_i} - \widetilde{\varphi}\widetilde{u}_i\right) = -\overline{\rho}D_{\text{SGS}}\frac{\partial\widetilde{\varphi}}{\partial x_i} \tag{7}$$

where φ denotes any scalar quantity, $D_{\text{SGS}} = \nu_{\text{SGS}}/\text{Sc}_{\text{SGS}}$ is the turbulent diffusivity and Sc_{SGS} denotes the turbulent Schmidt number. Finally, the unclosed expression of the SGS term in the filtered energy Equation (3) is given by:

$$\overline{(\rho e_t + p)u_j} - (\overline{\rho}\widetilde{e}_t + \overline{p})\widetilde{u}_j = \underbrace{\left[\overline{\rho c_p T u_j} - \overline{\rho}\,\overline{c_p}\widetilde{T}\widetilde{u}_j\right]}_{\mathcal{Q}_j} + \underbrace{\left[\frac{1}{2}\left(\overline{\rho u_i u_i u_j} - \overline{\rho}\widetilde{u}_i\widetilde{u}_i\widetilde{u}_j\right)\right]}_{\psi_{iij}} - \frac{1}{2}T_{ii}\widetilde{u}_j \tag{8}$$

where $\mathcal{Q}_j = -\lambda_{\text{SGS}}\partial\widetilde{T}/\partial x_j$ denotes the SGS heat flux also modeled with a gradient law, $\lambda_{\text{SGS}} = \mu_{\text{SGS}}\overline{c_p}/\text{Pr}_{\text{SGS}}$ is the turbulent thermal conductivity and Pr_{SGS} the turbulent Prandtl number. The quantity ψ_{ijk} denotes the triple velocity correlation tensor, which is closed by retaining the Daly and Harlow expression $\psi_{ijk} = C_{c3}\nu_{\text{SGS}}\partial T_{ij}/\partial x_k$ [9]. In the present study, the SGS eddy viscosity μ_{SGS} is expressed by the WALE (wall-adapting local eddy) model of Nicoud and Ducros [26]:

$$\mu_{\text{SGS}} = \overline{\rho}(C_w\Delta)^2\frac{(S_{ij}^d S_{ij}^d)^{3/2}}{(\widetilde{S}_{ij}\widetilde{S}_{ij})^{5/2} + (S_{ij}^d S_{ij}^d)^{5/4}} \tag{9}$$

where $C_w = C_s\sqrt{10.6}$ is the WALE model constant, Δ is the characteristic mesh size $\Delta = (\Delta x_1\Delta x_2\Delta x_3)^{1/3}$, and S_{ij}^d is the traceless symmetric part of the square of the resolved velocity gradient tensor:

$$S_{ij}^d = \frac{1}{2}\left(\frac{\partial\widetilde{u}_i}{\partial x_l}\frac{\partial\widetilde{u}_l}{\partial x_j} + \frac{\partial\widetilde{u}_j}{\partial x_l}\frac{\partial\widetilde{u}_l}{\partial x_i}\right) - \frac{1}{3}\frac{\partial\widetilde{u}_m}{\partial x_l}\frac{\partial\widetilde{u}_l}{\partial x_m}\delta_{ij} \tag{10}$$

2.2 Numerical methods

The main computational features of the massively-parallel `CREAMS` solver are as follows: the temporal integration is performed with an explicit third-order total-variation-diminishing (TVD) scheme [12]. The treatment of the inviscid components of the conservative vector fluxes is handled with the seventh-order accurate weighted essentially non oscillatory (WENO7) reconstruction of the characteristic fluxes [1], see reference [18]. In practice, the numerical solver uses the optimal seventh-order accurate flux reconstruction, and the application of the non-linear upwinding procedure is conditioned to a smoothness criterion that involves the local values of the normalized spatial variations of both pressure and density. The interested reader may find further details in the study of Buttay et al. [6]. The viscous and molecular diffusion fluxes are computed thanks to an eighth-order centered difference scheme.

`CREAMS` is coupled to the CVODE and EGLIB libraries [15, 10, 11], which allow detailed chemistry and multicomponent transport effects to be taken into account. As mentioned above, for the purpose of the present study, a mixture-average formulation based on a modified version of the Hirschfelder and Curtiss approximation has been retained. It corresponds to a first-order approximation of the most detailed transport representation provided by the EGLIB Library. Finally, a detailed verification of the solver may be found in reference [18], which gathers eight elementary verification subsets including, among others, the classical Sod's shock tube problem, the ignition sequence of a multi-species mixture in a shock tube, the unsteady diffusion of a smoothed concentration profile, and a one-dimensional laminar premixed flame. In the simulations reported below, the surface of the cavity is immersed into the Cartesian grid and a proper wall boundary condition must be imposed to the surrounding flow. This issue is addressed with the immersed boundary method (IBM) recently developed by Boukharfane et al. [5]. The main specificity of this method is that it combines direct-forcing and ghost-point forcing algorithms. Its performance has been previously assessed in many canonical compressible flows and reference benchmarks.

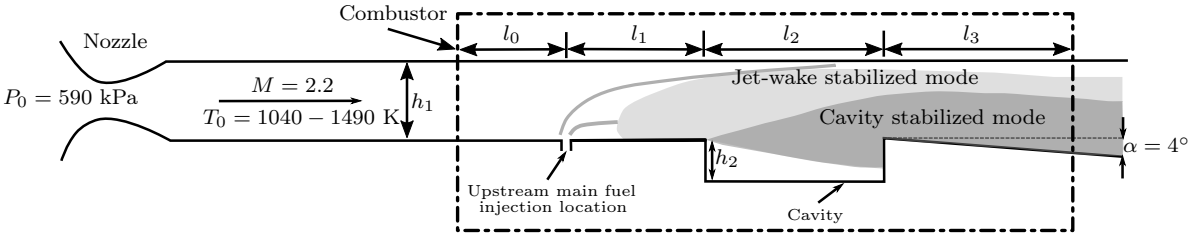

Figure 1: Schematics of the combustion facility studied by Micka and Driscoll [24]. The rectangular computational domain and its main characteristic dimensions are highlighted on the right side of the figure.

3 Computational setup and preliminary verifications

The experimental geometry under consideration corresponds to the supersonic combustion facility of the University of Michigan, which consists of a two-dimensional Mach 2.2 nozzle followed by a constant area isolator. This constant area section extends approximately 400 mm up to the leading edge of a rectangular cavity, which is 50.8 mm long, 12.7 mm high, and spans the width of the test section. It is followed by a 349 mm long and 4 degree diverging section, dumping into a 152 mm diameter exhaust, as shown in Figure 1, where the computational domain is presented. Room

temperature hydrogen is injected sonically on the combustor centerline at 44.5 mm upstream of the cavity leading edge through a single 2.50 mm diameter injection port. The initial air stagnation pressure is $P_0 = 590$ kPa, while the nominal value of the temperature T_0 may be varied. Two distinct values (1,100.0 K and 1,400.0 K) of the vitiated air-stream temperature are considered to study the combustion stabilization process (cases `RFSC-LST` and `RFSC-HST`).

The present set of computations is conducted within the large-eddy-simulation (LES) framework and the wall-adapting local eddy (WALE) model is retained as the subgrid-scale viscosity closure. Table 1 gathers the main parameters that characterize the vitiated air and hydrogen inlet streams in both cases. Hydrogen-air chemistry is represented with the detailed mechanism of O'Conaire et al. [27]. It consists of nine chemical species (H_2, O_2, H_2O, H, O, OH, HO_2, H_2O_2, and N_2) and 21 elementary reaction steps.

		case `RFSC-LST`	case `RFSC-HST`
Vitiated air inlet			
	Temperature (K)	1,100.0	1,400.0
	Y_{O_2} $(-)$	0.244	0.251
	Y_{N_2} $(-)$	0.671	0.607
	Y_{H_2O} $(-)$	0.085	0.142
Hydrogen inlet			
	Pressure (kPa)	845.0	755.0
	Y_{H_2} $(-)$	1.0	1.0

Table 1: Vitiated air and hydrogen inlet streams characteristics.

The computational domain can be decomposed into three distinct parts. The first consists of a constant section channel (*s1*) with length $L_{x_1,s1} = l_0 + l_1 = 94.5$ mm and height $L_{x_2,s1} = h_1 = 39.4$ mm, which is followed by a section (*s2*) of length $L_{x_1,s2} = l_2 = 50.8$ mm featuring the wall-mounted cavity of depth $h_2 = 12.7$ mm. Finally, the last section is the diverging one, it has a length $L_{x_1,s3} = l_3 = 76.2$ mm. The total length of the computational domain is thus $L_{x_1} = 221.5$ mm, while its dimension is $L_{x_3} = 38.1$ mm in the spanwise direction.

The computational grid is refined in the vicinity of hydrogen jet exit and at the location of the shear layer that develops above the cavity. The mesh is also refined near the walls. The total number of grid points is approximately 42,000,000. Several criteria have been used to check the quality of the resulting computational resolution, especially near the walls, which are modeled with the IBM algorithm. At some locations in the median plane along the spanwise direction (i.e., $x_3/D = 0$), the profiles of the logarithm of the viscosity ratio, i.e., $\log\left(\mu_{\texttt{SGS}}/\overline{\mu}\right)$, and normalized mean velocity u^+ have been extracted and plotted in walls units. The non-dimensional velocity u^+ is evaluated as the ratio between the local value of the mean longitudinal velocity component and friction velocity at the wall, i.e., $u^+ = u_1/u_{\tau_w}$. The wall distance is normalized by the ratio of the kinematic viscosity ν to the friction velocity u_{τ_w}, i.e., $y^+ = u_{\tau_w} y/\nu$, with y the distance perpendicular to the wall. The corresponding profiles confirm that, with the present level of resolution, despite a visible shift of the velocity in the logarithmic zone, the WALE model satisfactorily changes his behavior in the buffer layer that separates the logarithmic zone ($y^+ > 30.0$) from the viscous sublayer ($y^+ < 5.0$), see reference [26, 32] for further details. It is possible to verify that, in logarithmic coordinates, the viscosity ratio increases almost linearly – this is more visible in the case `RFSC-HST` – which is fully consistent with the data of the literature [26].

The assessment of the computational resolution is completed by proceeding with a mesh quality analysis. Two indexes of quality are therefore considered. Their values can vary between 0.0 and 1.0 ; the higher the value of the index, the better is the resolution. The first quality index under

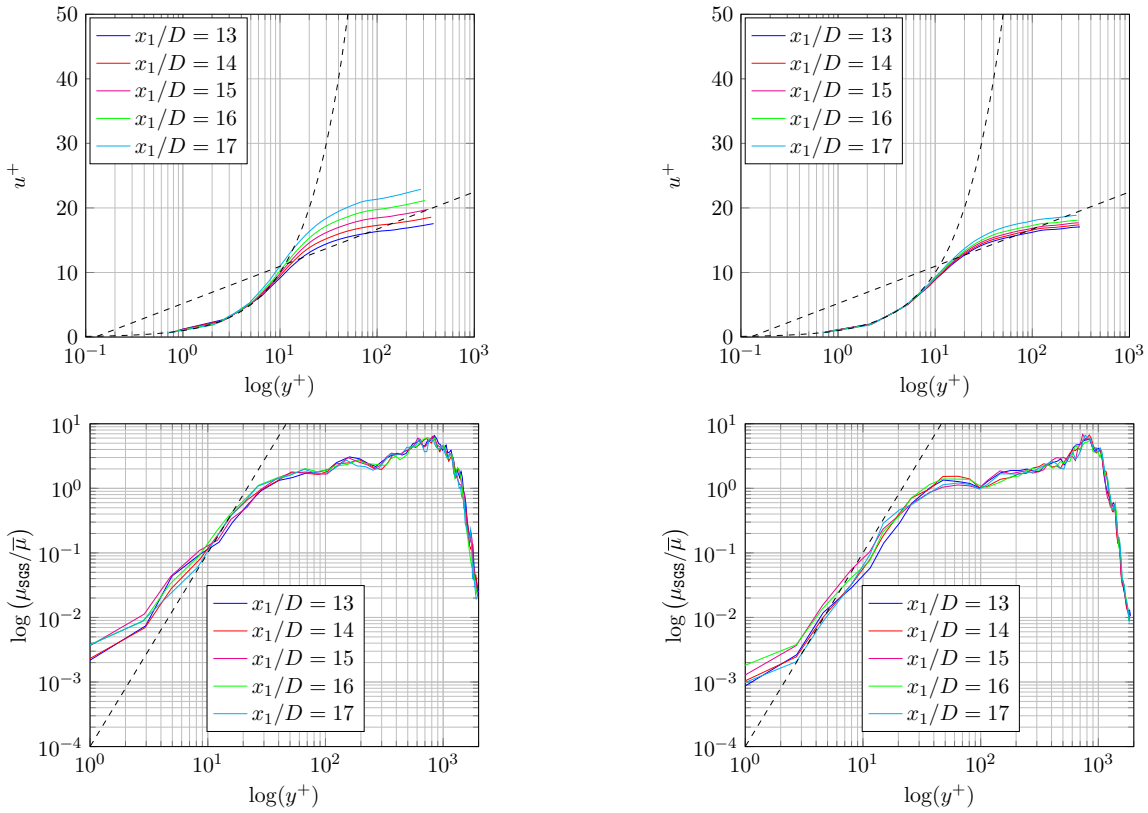

Figure 2: Mean velocity profile in wall units (top) and viscosity ratio (bottom) at several x_1/D locations in the median plane along the spanwise direction, i.e., $x_3/D = 0$. Left: case `RFSC-LST`, right: case `RFSC-HST`.

consideration is the modified quality index IQ_k of Pope [28]. It is based on a direct comparison between the resolved turbulent kinetic energy k and its subgrid-scale unresolved counterpart $k_{\mathtt{SGS}}$, which is evaluated from the Yoshizawa closure [35], i.e., $k_{\mathtt{SGS}} = \nu_{\mathtt{SGS}}^2/(C_M\Delta)^2$ with $C_M = 0.069$. The expression of IQ_k is given by $\mathrm{IQ}_k = k/(k + k_{\mathtt{SGS}})$. The analysis of the numerical resolution is also carried out by using the quality criterion proposed by Celik et al. [8]. It is based on a comparison between the computational grid characteristic size Δ and the Kolmogorov length scale $\mathcal{L}_\eta$

$$\mathrm{IQ}_\eta = \left(1 + \alpha_\eta \left(\Delta/\mathcal{L}_\eta\right)^m\right)^{-1}, \tag{11}$$

with $\left(\alpha_\eta, m\right) = (0.05, 0.5)$. The value of $\mathcal{L}_\eta$ is evaluated from the following scaling rule $\mathcal{L}_\eta = (\nu^3/\varepsilon)^{1/4}$ with ε the turbulent kinetic energy dissipation rate.

In this context, it seems worth recalling that a standard criterion for DNS computations is $k_{max}\mathcal{L}_\eta = 3/2$, in such a manner that, once k_{max} is approximated by π/Δ, such a criterion corresponds to $\Delta/\mathcal{L}_\eta$ approximately equal to 2.0, which leads to $\mathrm{IQ}_\eta = 0.93$. Thus, it seems that values of the quality index IQ_η larger than 0.93 are almost equivalent to the fulfilment of a standard DNS resolution criterion.

Figure 3 displays the PDF obtained with the two quality indexes. Provided that the modified quality index verifies $\mathrm{IQ}_k \geq 0.8$, the mesh resolution is considered to be sufficient since it means that at least 80% of the turbulent kinetic energy is captured at the resolved scale [28]. Because

the conclusions that may be drawn from the modified quality index are likely to be sensitive to the subgrid-scale modelling, it seems worthwhile to take a closer look at the behaviour obtained with the second quality index IQ_η. In this respect, Figure 3 shows that most of the values of the quality index IQ_η remain larger than 0.93. The CDF or cumulative distribution function $\mathbb{F}(x) = \int_0^x \mathtt{PDF}(\mathrm{IQ}_k)\mathrm{dIQ}_k$ that can be deduced from the probability density function indeed shows that almost 95 % of the obtained values are larger than this limit, see the plot reported on the right side of Figure 4.

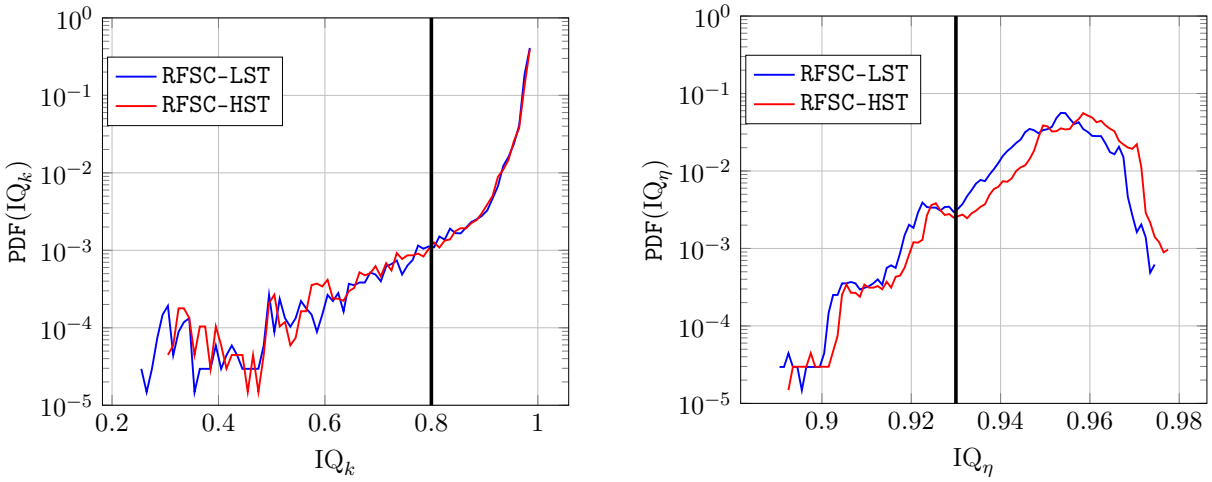

Figure 3: PDF of the quality index IQ_k and IQ_η obtained in the median plane along the spanwise direction, i.e., $x_3/D = 0$. Left: index IQ_k, right: index IQ_η.

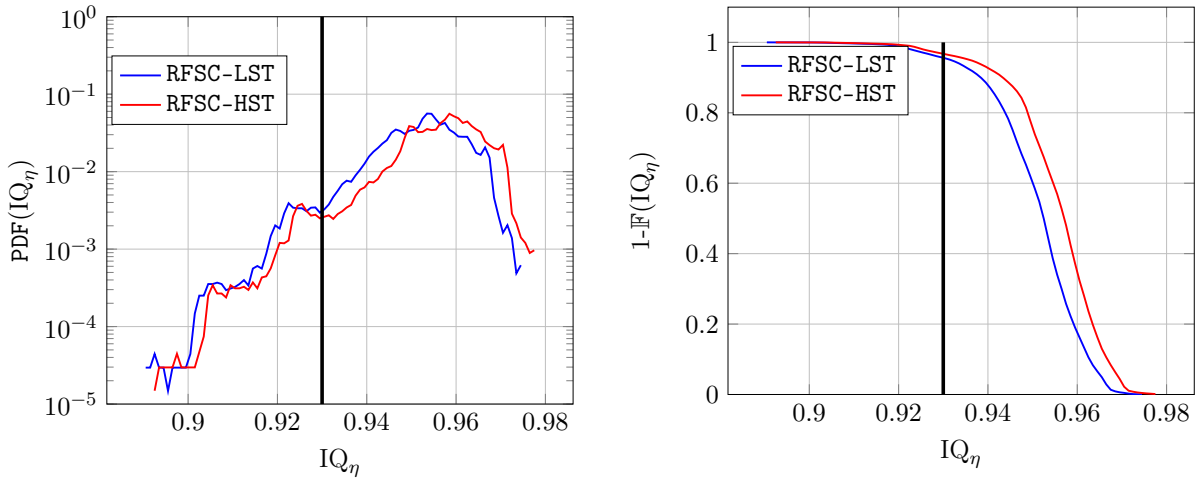

Figure 4: PDF of the quality index IQ_η (left) and value of 1-$\mathbb{F}(\mathrm{IQ}_\eta)$ (right), i.e., value of probability to have a value of the quality index larger than IQ_η.

Finally, it is quite interesting to check in Figure 5 that high values are also obtained in the vicinity of the hydrogen inlet stream and shear layer that develops above the wall-mounted cavity. Figure 5 indeed displays the results obtained in the median plane (i.e., $x_3/D = 0$) for both quality indexes. By analysing these images, one can notice that, upstream of the fuel inlet port, the level of resolution is excellent, while the quality criteria slightly decreases downstream of the hydrogen

injection. The decrease is more significant for the modified quality index IQ_k. However, even in this region, the corresponding values remain quite satisfactory since $IQ_k \geq 0.80$ and $IQ_\eta \geq 0.89$.

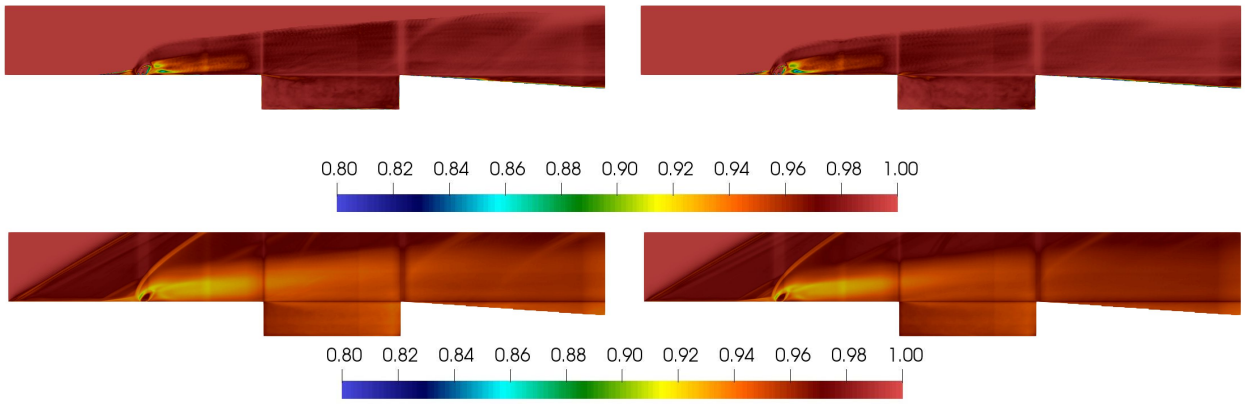

Figure 5: Fields of the quality indexes IQ_k and IQ_η obtained in the median plane along the spanwise direction, i.e., $x_3/D = 0$. Top: quality index IQ_k, bottom: quality index IQ_η. Left: case `RFSC-LST`, right: case `RFSC-HST`.

4 Detailed analysis of computational results

Figure 6 reports the temporal evolutions of the production rates of OH and H_2O in both cases `RFSC-LST` and `RFSC-HST`. For the simulation case `RFSC-LST`, chemical reactions are initiated at the bottom end of the wall-mounted cavity. According to the OH formation, the reaction first develops within the cavity, leading to a temperature increase and a deflection of the shear layer induced by the associated heat release. As the combustion processes develop, the conditions become more favorable to the spreading of chemical reactions, thus increasing the temperature and allowing the reaction zone to extend to the whole cavity. Eventually, the heat release rate becomes sufficient to stabilize the combustion process and, depending on the operating conditions, it can spread upstream of the cavity, as it is seen for case `RFSC-HST`. However, it is noteworthy that the vitiated air inlet temperature affects significantly the stabilization mode. It is also to be noted that, with a higher temperature, the combustion spreads significantly faster, as it can be verified by OH mass fraction and H_2O production rate reported in Figures 6 and 7. Moreover, Figure 7 shows that, for the cavity-stabilized combustion mode (case `RFSC-LST`), significant H_2O production takes place along the upper part of the cavity, whereas for the jet-wake stabilized mode (case `RFSC-HST`) it tends to spread just downstream of the hydrogen injection and within the cavity.

The analysis of the reactive flowfields confirms the occurrence of two distinct stabilization modes: a cavity-stabilized mode is dominant for moderate values of the airstream stagnation temperature (case `RFSC-LST`), while non-negligible water vapor dissociation and heat release occur in the vicinity of the hydrogen release for larger inlet temperature values (case `RFSC-HST`), as shown in Figure 8, which reports instantaneous snapshots of the iso-surface $\widetilde{\xi} = 0.5$ of the filtered fuel inlet tracer $\widetilde{\xi}$ (in light grey) as well as an isovalue of the OH filtered mass fraction colored by the filtered temperature. As expected, case `RFSC-HST` displays a higher amount of OH inside the wall-mounted cavity but besides that, there is a non-negligible presence of OH upstream of the cavity and in the direct vicinity of the H_2 jet injection, while for case `RFSC-LST` OH radical tends to remain confined within the cavity and further downstream.

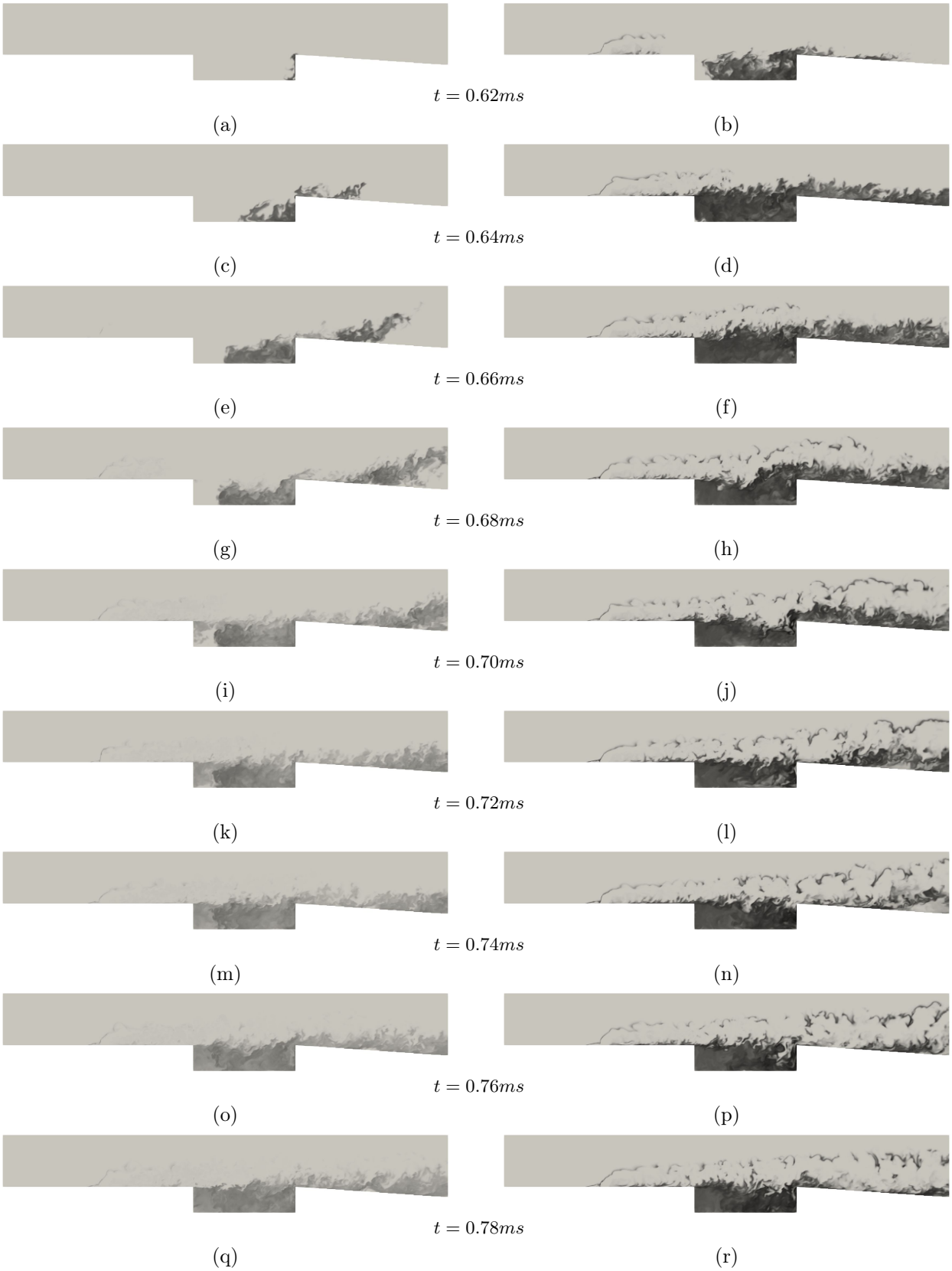

Figure 6: Temporal evolution of the production rates of OH for case `RFSC-LST` (left) and case `RFSC-HST` (right).

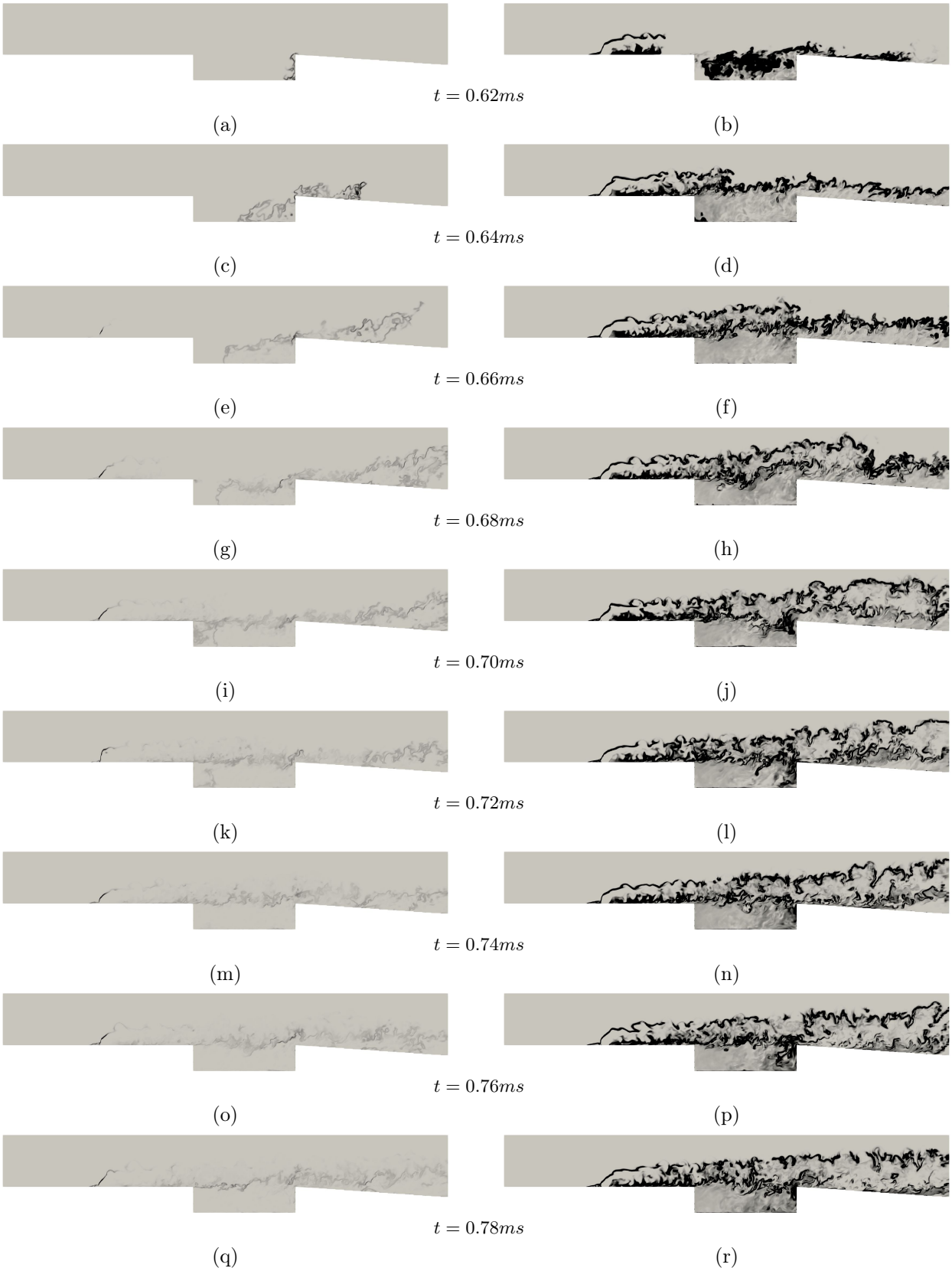

Figure 7: Temporal evolution of the production rates of H_2O for case `RFSC-LST` (left) and case `RFSC-HST` (right).

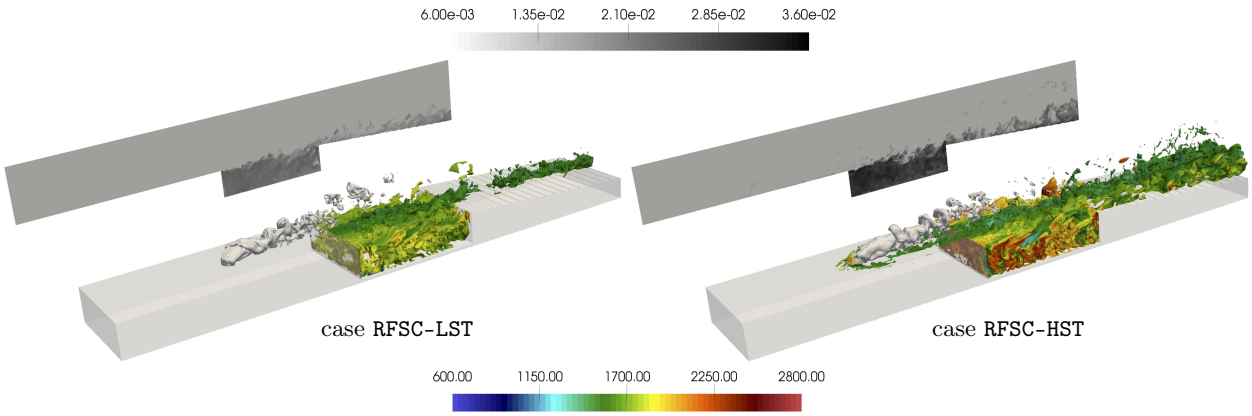

Figure 8: Iso-value surface of the OH filtered mass fraction colored by the filtered temperature (in Kelvin) and fuel inlet tracer iso-surface $\widetilde{\xi} = 0.5$ in light grey. Back side: OH mass fraction.

One of the main characteristics of the cavity stabilized combustion mode is that the reaction zone is anchored at the leading edge of the cavity and spreads into the main flow at an approximately constant angle, whereas for jet-wake stabilized mode the reaction zone is stabilized upstream of the cavity and the leading edge is curved. These results appear to be similar to the ones previously obtained by Lin et al. [17], Mathur et al. [21], and Micka [22] for cavity-stabilized combustion mode, as it can be verified in Figure 9.

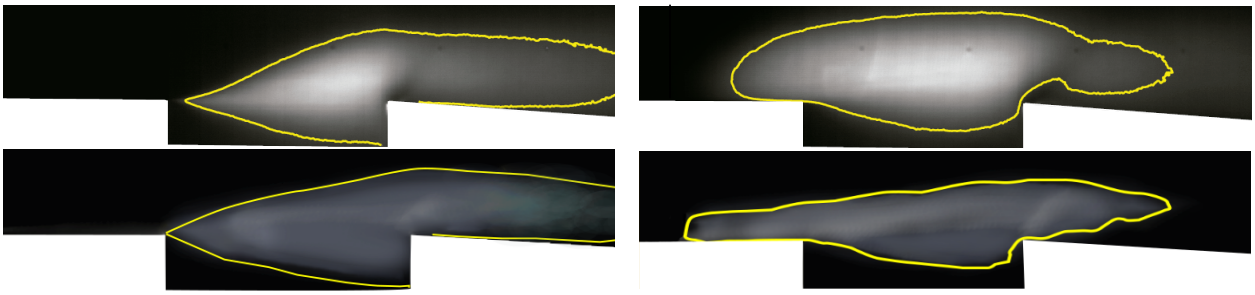

Figure 9: Comparisons between flame luminosity adapted from Micka [22] (top) and averaged heat release rate (bottom). Left: cavity-stabilized mode `RFSC-LST`. Right: jet-wake stabilized mode `RFSC-HST`.

Since a non-negligible amount of chemical reaction takes place rather far downstream of the fuel injection, it would be interesting to discriminate the contributions of premixed and non-premixed (i.e., diffusive) combustion modes in this peculiar geometry.

To this purpose, a premixedness index is considered. It is defined as follows:

$$\zeta_p = \frac{1}{2}\left(1 + \boldsymbol{n}_F \cdot \boldsymbol{n}_O\right) \tag{12}$$

where $\boldsymbol{n}_F$ denotes a normal unit vector associated to the molecular diffusion flux of the fuel, while $\boldsymbol{n}_O$ is the one related to oxygen. These normal unit vectors can be determined directly from the molecular diffusion velocities, i.e., $\boldsymbol{V}_F$ and $\boldsymbol{V}_O$, as suggested by Buttay et al. [7], or approximated by the species mass fraction gradients, as early proposed by Takeno and coworkers [34], which is fully consistent with a Fickian representation of molecular transport.

As it is defined above, the value of this premixedness index is expected to approach unity for premixed combustion conditions and zero for diffusive ones. It should be noted that, as previously discussed in reference [20], there exist special situations where the representativeness of such a premixedness index can be questioned. However, despite these limitations, it should be emphasized that it is very easy to evaluate and remains largely used to proceed with a preliminary inspection of partially-premixed combustion characteristics.

This index is presently evaluated with $\boldsymbol{n}_F = \boldsymbol{\nabla}\widetilde{Y}_F / \left\| \boldsymbol{\nabla}\widetilde{Y}_F \right\|$ and $\boldsymbol{n}_O = \boldsymbol{\nabla}\widetilde{Y}_O / \left\| \boldsymbol{\nabla}\widetilde{Y}_O \right\|$ for both cases `RFSC-LST` and `RFSC-HST`. The post-processing of ζ_p confirms that, in both cases, the contributions of premixed and diffusive modes are both significant. A premixed flame structure develops in the vicinity of the leading edge of the wall-mounted cavity and supports the diffusive combustion contribution. Figure 10 presents the `PDF` of the premixedness index ζ_p at various times $t = 1.1$ ms, 1.2 ms, 1.3 ms, and 1.4 ms for a volume restricted to $0.001 \leq \xi \leq 0.999$ and featuring non-negligible values of the heat release rate.

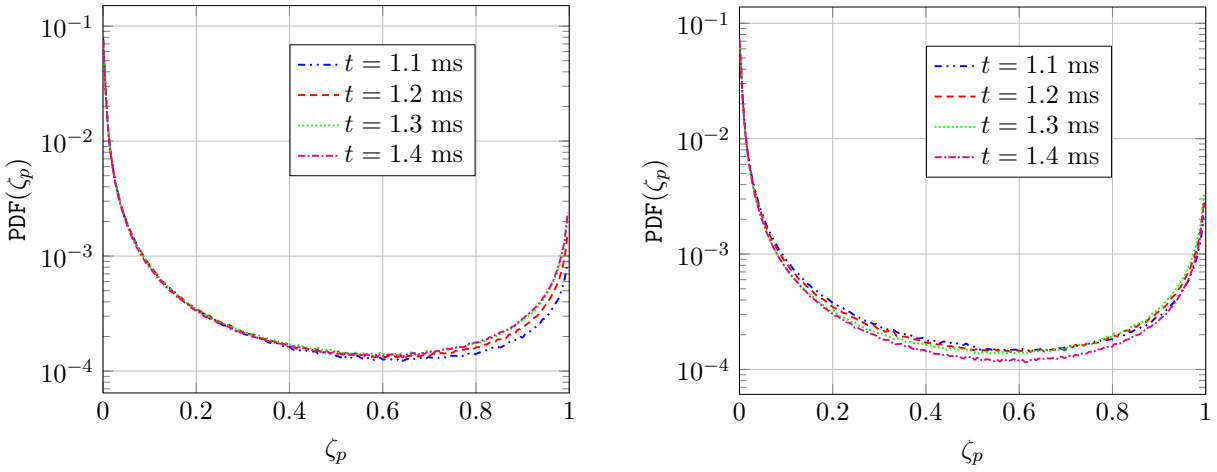

(a) Case `RFSC-LST` (b) Case `RFSC-HST`

Figure 10: PDF of the premixedness index ζ_p

Finally, since there is a non-negligible amount of chemical reactions that take place in a premixed combustion mode, the present study is ended by an analysis of the turbulent premixed combustion regimes. These regimes are analysed in the standard combustion diagram of Barrère and Borghi [3, 4] using the normalized length scale ratio $\mathcal{L}_t/\delta_L^0$ and normalized velocity ratio $u_{\texttt{RMS}}/S_L^0$ as the relevant set of coordinates. Turbulent time and length scales are estimated on the basis of the homogeneous isotropic turbulence (HIT) assumption, $u_{\texttt{RMS}} = \sqrt{2k/3}$ and $\mathcal{L}_t = u_{\texttt{RMS}}^3/\varepsilon$, with $k = \overline{\rho u_i'' u_i''}/(2\,\overline{\rho})$ the turbulent kinetic energy and ε its dissipation rate.

The unstrained laminar premixed flame characteristics are estimated from the local conditions at the pressure, temperature, equivalence ratio, and temperature of the corresponding unburnt mixtures. The corresponding quantities S_L^0 and δ_L^0 are calculated at each point under the following conditions: (i) the point lies inside a zone where the probability to have a premixed flame structure remains larger than a given threshold value (10% here) and, in terms of mixture fraction or corresponding equivalence ratio, (ii) the value of ξ remains within a range where the propagation of a premixed flame may occur, i.e., within the lean and rich flammability limits.

From Figure 11 one can notice that, for both cases, there is a large variability of premixed combustion regimes, including wrinkled flamelets, thickened-wrinkled flames, thickened flames, and

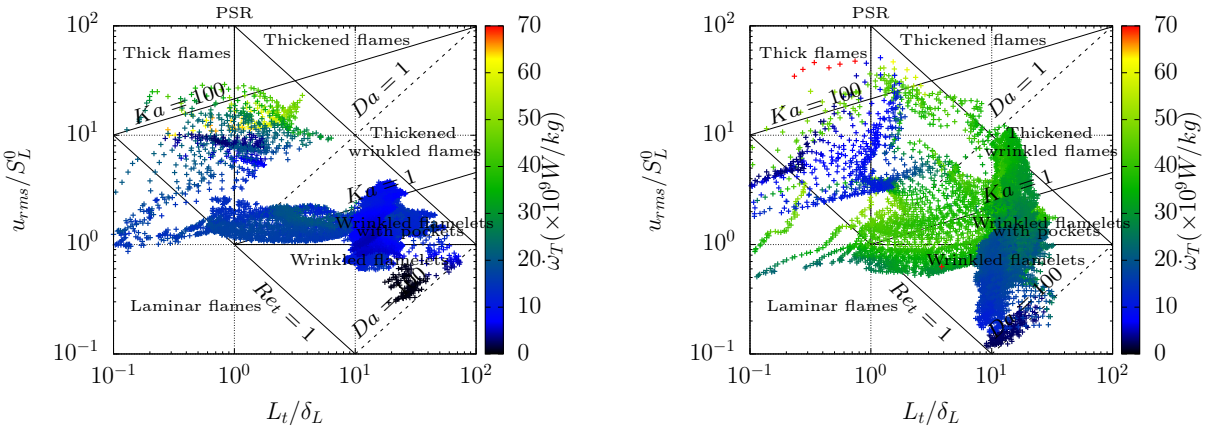

(a) Case RFSC-LST

(b) Case RFSC-HST

Figure 11: Premixed turbulent combustion diagram based on the Borghi-Barrère coordinates [4].

even possible incursions in laminar flame combustion regimes. For the case `RFSC-LST`, most of the points are located in the vicinity of the flamelet regime, between the Klimov-Williams limit ($Ka = 1$) and the horizontal line corresponding to $u_{\mathtt{RMS}}/S_L^0 = 1.0$. There is also a very small amount of points featuring a non-negligible heat release rate that are located in the thickened flame region. In case `RFSC-HST`, it is remarkable that the characteristic values of the heat-release rate (HRR) are significantly higher. The location of these points characterized by larger HRR values tends to spread towards the thickened-wrinkled and thickened flame regimes, which correspond to smaller Damköhler number and larger Karlovitz number values. Non-negligible finite-rate chemistry effects come into play.

5 Conclusions and future works

Flame stabilization mechanism and turbulence-chemistry interactions are studied for a jet in a supersonic crossflow (JISCF) of vitiated air delivering hydrogen upstream of a squared cavity. The conditions are relevant to experiments previously conducted at the University of Michigan [22, 24]. The computations are performed with the high-performance computational solver `CREAMS` [18, 19] and makes use of a recent immersed boundary method (IBM) algorithm [5]. The present set of computations is conducted within the LES framework and the wall-adapting local eddy (WALE) model is retained as the subgrid-scale viscosity closure. Several criteria are used to check the computational resolution, especially near the walls, which are represented through an IBM, where some efforts have been spent to capture the flow as accurately as possible. The use of the WALE model allows to satisfactorily recover the behavior in the buffer layer that separates the logarithmic zone from the viscous sublayer.

Depending on the inlet vitiated airstream temperature, two stabilization modes are recovered: cavity-stabilized regime and jet-wake stabilized regime. In the cavity stabilized combustion mode, combustion is anchored at the leading edge of the wall-mounted cavity and spreads into the main flow at an approximately constant angle, whereas jet-wake stabilized combustion takes place directly downstream of the fuel injection, i.e., upstream of the cavity. In this respect, it seems worth mentioning that different averaged streamline flowfields – not reported for the sake of conciseness – have been obtained for cavity and jet-wake stabilization modes. For high operative temperatures, combustion primarily takes place in the jet-wake stabilization mode while, for lower operative tem-

peratures, the cavity stabilization mode is obtained. This is fully consistent with the experimental results of Micka and Driscoll [23]. For intermediate values of the operative temperature, some oscillations between the two modes are expected and it would be interesting to run complementary numerical simulations at these intermediate operative temperatures so as to understand how these oscillations may happen and how long each stabilization mode is active. The analysis of combustion regimes confirms the occurrence of highly turbulent premixed flame conditions. In this respect, a perspective for future works concerns the representation of turbulence-chemistry interactions and the resort to modelling proposals suited to such conditions. This is the matter of our current work following the previous efforts done in this direction by Moule et al. [25] and Techer [31].

6 Acknowledgments

This study is a part of the Ph.D. Thesis of F.H. Eugênio Ribeiro, which is financially supported by the Brazilian program Ciência sem Fronteiras of CNPq and Brazilian Air Force. F.H. Eugênio Ribeiro is indebted to Dr. Anthony Techer and Aimad Er-Raiy for many stimulating discussions on tricky technical issues. This work was granted access to the HPC resources of CINES, IDRIS, and TGCC under the allocations x20152b7456 and i20152b7251.

References

[1] Balsara, D. and Shu, C. (2000). Monotonicity preserving weighted essentially non-oscillatory schemes with increasingly high-order of accuracy. *Journal of Computational Physics*, 106:405–452.

[2] Ben-Yakar, A. and Hanson, R. K. (2001). Cavity flame-holders for ignition and flame stabilization in scramjets: an overview. *Journal of propulsion and power*, 17(4):869–877.

[3] Borghi, R. (1984). Mise au point sur la structure des flammes turbulentes. *Journal de Chimie Physique*, 81:361–370.

[4] Borghi, R. (1985). On the structure and morphology of turbulent premixed flames. In Casci, C., editor, *Recent Advances in the Aerospace Science*, pages 117–138. Plenum Publishing.

[5] Boukharfane, R., Ribeiro, F., Bouali, Z., and Mura, A. (2018). A combined ghost-point-forcing / direct-forcing immersed boundary method for compressible flow simulations. *Computers & Fluids*, 162:91–112.

[6] Buttay, R., Lehnasch, G., and Mura, A. (2016). Analysis of small-scale scalar mixing processes in highly under-expanded jets. *Shock Waves*, 26:193–212.

[7] Buttay, R., Lehnasch, G., and Mura, A. (2017). Highly resolved numerical simulation of combustion downstream of a rocket engine igniter. *Shock Waves*, 27:655–674.

[8] Celik, I., Cehreli, Z., and Yavuz, I. (2005). Index of resolution quality for large eddy simulations. *Journal of fluids engineering*, 127(5):949–958.

[9] Daly, B. J. and Harlow, F. H. (1970). Transport equations in turbulence. *The Physics of Fluids*, 13(11):2634–2649.

[10] Ern, A. and Giovangigli, V. (1994). *Multicomponent transport algorithms*, volume 24. Springer Science & Business Media.

[11] Ern, A. and Giovangigli, V. (1995). Fast and accurate multicomponent transport property evaluation. *Journal of Computational Physics*, 120:105–116.

[12] Gottlieb, S. and Shu, C. W. (1998). Total variation diminishing runge-kutta schemes. *Mathematics of computation of the American Mathematical Society*, 67(221):73–85.

[13] Gruber, M. R., Donbar, J. M., Carter, C. D., and Hsu, K.-Y. (2004). Mixing and combustion studies using cavity-based flameholders in a supersonic flow. *Journal of Propulsion and Power*, 20(5):769–778.

[14] Heiser, W. H. and Pratt, D. T. (1994). *Hypersonic airbreathing propulsion*. AIAA.

[15] Hindmarsh, A. C., Brown, P. N., Grant, K. E., Lee, S. L., Serban, R., Shumaker, D. E., and Woodward, C. S. (2005). Sundials: Suite of nonlinear and differential/algebraic equation solvers. *ACM Transactions on Mathematical Software (TOMS)*, 31(3):363–396.

[16] Hirschfelder, J. O. and Curtiss, C. F. (1949). The theory of flame propagation. *The Journal of Chemical Physics*, 17(11):1076–1081.

[17] Lin, K.-C., Tam, C.-J., Boxx, I., Carter, C., Jackson, K., and Lindsey, M. (2007). Flame characteristics and fuel entrainment inside a cavity flame holder of a scramjet combustor. In *43rd AIAA/ASME/SAE/ASEE Joint Propulsion Conference & Exhibit*, page 5381.

[18] Martínez-Ferrer, P., Buttay, R., Lehnasch, G., and Mura, A. (2014). A detailed verification procedure for compressible reactive multicomponent Navier-Stokes solvers. *Computers & Fluids*, 89:88–110.

[19] Martínez-Ferrer, P., Lehnasch, G., and Mura, A. (2017a). Compressibility and heat release effects in high-speed reactive mixing layers i.: Growth rates and turbulence characteristics. *Combustion and Flame*, 180:284–303.

[20] Martínez-Ferrer, P., Lehnasch, G., and Mura, A. (2017b). Compressibility and heat release effects in high-speed reactive mixing layers. part ii. structure of the stabilization zone and modeling issues relevant to turbulent combustion in supersonic flows. *Combustion and Flame*, 180:304–320.

[21] Mathur, T., Gruber, M., Jackson, K., Donbar, J., Donaldson, W., Jackson, T., and Billig, F. (2001). Supersonic combustion experiments with a cavity-based fuel injector. *Journal of Propulsion and Power*, 17(6):1305–1312.

[22] Micka, D. (2010). *Combustion stabilization, structure, and spreading in a laboratory dual-mode scramjet combustor*. PhD thesis, University of Michigan.

[23] Micka, D. and Driscoll, J. (2008). Dual-mode combustion of a jet in cross-flow with cavity flameholder. In *46th AIAA Aerospace Sciences Meeting and Exhibit*, page 1062.

[24] Micka, D. and Driscoll, J. (2009). Combustion characteristics of a dual-mode scramjet combustor with cavity flameholder. *Proceedings of the combustion institute*, 32(2):2397–2404.

[25] Moule, Y., Sabelnikov, V., and Mura, A. (2014). Highly resolved numerical simulation of combustion in supersonic hydrogen-air coflowing jets. *Combustion and Flame*, 161(10):2647–2668.

[26] Nicoud, F. and Ducros, F. (1999). Subgrid-scale stress modelling based on the square of the velocity gradient tensor. *Flow, Turbulence and Combustion*, 62(3):183–200.

[27] Ó Conaire, M., Curran, H. J., Simmie, J. M., Pitz, W. J., and Westbrook, C. K. (2004). A comprehensive modeling study of hydrogen oxidation. *International Journal of Chemical Kinetics*, 36(11):603–622.

[28] Pope, S. B. (2004). Ten questions concerning the large-eddy simulation of turbulent flows. *New journal of Physics*, 6(1):35.

[29] Ribeiro, F. and Leite, V. (2012). Evaluation of a vitiated air generator conditions for the 14-X vehicle combustor tests. *Proceedings of the 14th Brazilian Congress of Thermal Science and Engineering, Rio de Janeiro*.

[30] Sun, M., Geng, H., Liang, J. H., and Wang, Z. G. (2008). Flame characteristics in supersonic combustor with hydrogen injection upstream of cavity flameholder. *Journal of Propulsion and Power*, 24(4):688–696.

[31] Techer, A. (2017). *Simulation aux grandes échelles implicite et explicite de la combustion supersonique*. PhD thesis, ISAE-ENSMA École Nationale Supérieure de Mécanique et d'Aérotechique - Poitiers.

[32] Techer, A., Moule, Y., Lehnasch, G., and Mura, A. (2018). Mixing of a fuel in a supersonic crossflow: Estimation of subgrid-scale scalar fluctuations. *AIAA Journal*, 56(2):465–481.

[33] Urzay, J. (2018). Supersonic combustion in air-breathing propulsion systems for hypersonic flight. *Annual Review of Fluid Mechanics*, 50:593–627.

[34] Yamashita, H., Shimada, M., and Takeno, T. (1996). A numerical study on flame stability at the transition point of jet diffusion flames. *Symposium (International) on Combustion*, 26:27–34.

[35] Yoshizawa, A. (1986). Statistical theory for compressible turbulent shear flows, with the application to subgrid modeling. *Physics of Fluids*, 29:2152–2164.